UC San Diego
UC San Diego Previously Published Works

Title

Pattern formation by phase-field relaxation of bending energy with fixed surface area and volume

Permalink

https://escholarship.org/uc/item/4wd9p8tq

Journal

Physical Review E, 90(3)

ISSN

2470-0045

Authors

Banham, Timothy
Li, Bo
Zhao, Yanxiang

Publication Date

2014-09-01

DOI

10.1103/physreve.90.033308

Peer reviewed

Pattern Formation by Phase-Field Relaxation of Bending Energy with Fixed Surface Area and Volume

Timothy Banham[*],
West Virginia Wesleyan College (WVWC), 59 College Ave, Buckhannon, WV 26201, USA

Bo Li[†], and
Department of Mathematics and Center for Theoretical Biological Physics, University of California, San Diego, 9500 Gilman Drive, MC 0112, La Jolla, CA 92093-0112, USA

Yanxiang Zhao[‡]
Department of Mathematics, the George Washington University, Washington, DC 20052, USA

Abstract

We explore a wide variety of patterns of closed surfaces that minimize the elastic bending energy with fixed surface area and volume. To avoid complicated discretization and numerical instabilities for sharp surfaces, we reformulate the underlying constrained minimization problem by constructing phase-field functionals of bending energy with penalty terms for the constraints, and develop stable numerical methods to relax these functionals. We report our extensive computational results with different initial surfaces. These results are discussed in terms of the reduced volume, and are compared with the known results obtained using the sharp-interface approach. Finally, we discuss the implications of our numerical findings.

I. INTRODUCTION

Bending energy contributes crucially to physical and biological properties of closed surfaces. Examples of such properties in biology include the biconcave shape of a red blood cell and the different equilibrium states of cell membranes [1–6]. Macroscopically the bending energy of a closed surface is often modeled by the surface integral of the square of mean curvature (i.e., the average of two principal curvatures). This integral is the principal term in the widely used Canham–Helfrich functional, an integral over the surface of a quadratic polynomial of mean curvature [1, 7]. One of the interesting problems related to the interfacial phenomenon is the minimization of bending energy with fixed surface area and enclosed volume [6, 8, 9]. In this work, we study numerically such a problem to explore a variety of different patterns.

The numerical implementation for minimizing the bending energy of closed surfaces, with or without constraints, is in general very challenging as it amounts to solving a problem of

---

[*]Electronic address: banham_t@wvwc.edu
[†]Electronic address: bli@math.ucsd.edu
[‡]Electronic address: y1zhao@ucsd.edu

geometrical flow, the Willmore flow [10]. This is a nonlinear fourth-order partial differential equation. With a usual sharp-interface formulation and a fixed finite-difference spatial grid, the numerical discretization of such an equation can be very complicated and the stability of numerical solution is hard to achieve. An alternative approach is to use a phase-field representation of the surface [11–13]. This means that a phase field, a continuous function defined on the entire computational domain, takes values close to one constant (say, 0) outside the closed surface and another constant (say, 1) inside, but smoothly varies its values from one of the constants to another in a thin transition region that represents the surface. Such an approach has been widely used in studying surface and interface problems arising in many scientific areas, such as materials physics, complex fluids, and biomolecular systems, cf. [11–27] and the references therein.

In our current work, we develop a phase-field model to minimize the bending energy of a closed surface with fixed surface area and enclosed volume. We use the phase-field description of the bending energy that has been mathematically analyzed thoroughly in [28–31]. We enforce the surface-area and volume constraints by penalty terms. This is similar in part to the method used in [30] but is different from some other methods, such as the Lagrange multipliers method used in [22, 31, 32]. In [31], the volume constraint results from a Model-B-like formulation of the underlying relaxation dynamics, involving high-order spatial derivatives. One of the reasons that we use penalty terms is for easier numerical implementation. We minimize our phase-field functional by solving the gradient-flow partial differential equations, using a finite-difference spectral method. We report our extensive numerical results of a wide variety of equilibrium patterns resulting from minimizing the bending energy with fixed surface area and enclosed volume in three-dimensional space (or fixed perimeter and enclosed area in two-dimensional space). In three-dimensional space which is of most practical interest, these patterns are analyzed using the reduced volume (i.e., the ratio of volume to that of the unit ball). In particular, we compare our results with the known, sharp-interface results for the three-dimensional axisymmetric case [8].

The rest of this paper is organized as follows: In Section II, we describe our phase-field energy functionals and the related gradient flows. In Section III, we present briefly our numerical methods. In Section IV, we report and analyze our computational results. Finally, in Section V, we draw conclusions.

II. PHASE-FIELD ENERGY FUNCTIONAL AND RELATED GRADIENT FLOW

We consider the minimization of bending energy of closed surfaces, possibly with multiple connected components, that have fixed surface area A and fixed volume V enclosed by the surface, where A and V are two positive constants. Let ε be a positive number such that $\varepsilon \ll 1$. Let Ω denote our computational domain in $\mathbb{R}^2$ or $\mathbb{R}^3$. We define the phase-field functional of all smooth functions $u = u(x)$ $(x \in \Omega)$

$$E_\varepsilon[u] = \int_\Omega \frac{\kappa}{2\varepsilon} \left[-\varepsilon\Delta u + \frac{1}{\varepsilon} W'(u) \right]^2 \mathrm{d}x + \frac{1}{2} M_A(\varepsilon) \left[A_\varepsilon(u) - A \right]^2 + \frac{1}{2} M_V(\varepsilon) \left[V_\varepsilon(u) - V \right]^2, \quad \text{(II.1)}$$

where

$$A_\varepsilon(u) = \int_\Omega \left[\frac{\varepsilon}{2} |\nabla u|^2 + \frac{1}{\varepsilon} W(u) \right] \, dx, \quad \text{(II.2)}$$

$$V_\varepsilon(u) = \int_\Omega u(x) \, dx. \quad \text{(II.3)}$$

The first term in (II.1) approximates the bending energy. In this term, the parameter $\kappa > 0$ is the bending modulus, and

$$W(u) = 18 u^2 (1-u)^2 \quad \text{(II.4)}$$

is a double-well potential with the "two wells" 0 and 1. The second term in (II.1) is a penalty term. It enforces the surface area to be A. The quantity $M_A(\varepsilon)$ is a function of ε such that $M_A(\varepsilon) > 0$ and $M_A(\varepsilon) \to \infty$ as $\varepsilon \to 0$. The term $A_\varepsilon(u)$ defined in (II.2) is a phase-field description of the area of interface separating the regions where a phase field u takes the values 0 and 1, respectively. With the prefactor chosen precisely to be 18 in (II.4), it is known that $A_\varepsilon[u]$ converges (in certain sense of functional convergence called Γ-convergence) to the surface area in the sharp-interface limit (i.e., in the limit $\varepsilon \to 0$) [33–35]. The third term in (II.1) is also a penalty term. It enforces the volume to be V, since $V_\varepsilon(u)$ defined in (II.3) approximates the volume of the region defined by $u \approx 1$. The quantity $M_V(\varepsilon)$ is positive, and depends also on ε. Moreover, $M_V(\varepsilon) \to \infty$ as $\varepsilon \to 0$.

Heuristically, if the first term (the integral term) in the functional $E_\varepsilon[u]$ is small, then the integrand will be close to 0. That means u solves approximately the Euler–Lagrange equation corresponding to the variational problem of minimizing $A_\varepsilon(u)$ that is defined in (II.2). This minimization leads to $W(u) \approx 0$ for $\varepsilon \ll 1$. Therefore, $u \approx 1$ or 0 in Ω. Mathematical studies indicate that $A_\varepsilon(u)$ is now close to the interfacial area and $V_\varepsilon(u)$ is close to the volume of the region where $u \approx 1$ [33–35].

To minimize the functional (II.1), we consider the relaxation dynamics, i.e., the gradient flow

$$\frac{\partial u}{\partial t} = -M(\varepsilon) \frac{\delta E_\varepsilon}{\delta u}, \quad \text{(II.5)}$$

where t is the time, $M(\varepsilon) > 0$ is a mobility constant that can depend on ε, and $\delta E_\varepsilon / \delta u$ is the variational derivative of E_ε. Direct calculations lead to

$$\frac{\delta E_\varepsilon}{\delta u} = \frac{\kappa}{\varepsilon} \left[\varepsilon \Delta - \frac{1}{\varepsilon} W''(u) \right] \left[\varepsilon \Delta u - \frac{1}{\varepsilon} W'(u) \right] + M_A(\varepsilon) \left[A_\varepsilon(u) - A \right] \left[-\varepsilon \Delta u + \frac{1}{\varepsilon} W'(u) \right] + M_V(\varepsilon) \left[V_\varepsilon(u) - V \right]. \quad \text{(II.6)}$$

Combining (II.5) and (II.6), we therefore obtain the time-dependent equation that we need to solve

$$\frac{\partial u}{\partial t} = -\frac{M(\varepsilon)\kappa}{\varepsilon} \left[\varepsilon\Delta - \frac{1}{\varepsilon}W''(u) \right] \left[\varepsilon\Delta u - \frac{1}{\varepsilon}W'(u) \right]$$
$$- M(\varepsilon)M_{\mathrm{A}}(\varepsilon)\left[A_{\varepsilon}(u) - A\right] \left[-\varepsilon\Delta u + \frac{1}{\varepsilon}W'(u) \right] - M(\varepsilon)M_{\mathrm{V}}(\varepsilon)\left[V_{\varepsilon}(u) - V\right]. \tag{II.7}$$

We choose our computational domain Ω to be a box in $\mathbb{R}^2$ or $\mathbb{R}^3$, and use the periodic boundary condition. Initial solutions $u^{(0)} = u^{(0)}(x)$ $(x \in \Omega)$ will be specified in the numerical computation. As the functional E_{ε} is highly nonconvex, different initial solutions can lead to different final, stable, steady-state solutions that are local minimizers of the functional E_{ε}.

III. NUMERICAL METHODS

In this section, we describe briefly our numerical methods for solving the gradient-flow equation (II.7). We present our methods for the three-dimensional case and omit those, similar and simpler, for the two-dimensional case. We choose our computational box to be a cube $(-L/2, L/2) \times (-L/2, L/2) \times (-L/2, L/2)$ for some $L > 0$ and cover it by a uniform finite-difference grid with grid size h in each direction. We choose a time step $\Delta t > 0$ and denote $t_m = m\,\Delta t$ $(m = 0, 1, \ldots)$. For a given function $u(x, t)$, we denote by $u^{(m)} = u^{(m)}(x)$ an approximation of $u(x, t_m)$.

We rewrite Eq. (II.7) into

$$\frac{\partial u}{\partial t} = -\varepsilon M(\varepsilon)\kappa\Delta^2 u + B[u],$$

where

$$B[u] = \frac{M(\varepsilon)\kappa}{\varepsilon} \left[\Delta(W'(u)) + W''(u)\Delta u - \frac{1}{\varepsilon^2}W'(u)W''(u) \right]$$
$$- M(\varepsilon)M_{\mathrm{A}}(\varepsilon)\left[A_{\varepsilon}(u) - A\right] \left[-\varepsilon\Delta u + \frac{1}{\varepsilon}W'(u) \right] - M(\varepsilon)M_{\mathrm{V}}(\varepsilon)\left[V_{\varepsilon}(u) - V\right].$$

We design accordingly our semi-implicit splitting scheme to discretize the time variable for Eq. (II.7):

$$\frac{u^{(m+1)} - u^{(m)}}{\Delta t} = -\varepsilon M(\varepsilon)\kappa\Delta^2 u^{(m+1)} + B\left[u^{(m)}\right], \quad m = 0, 1, \ldots,$$

where $u^{(0)}$ is a given initial solution. Here all the nonlinear terms, collected in the B term, are treated explicitly. Rearranging terms, we obtain

$$u^{(m+1)} + \Delta t\varepsilon M(\varepsilon)\kappa\Delta^2 u^{(m+1)} = u^{(m)} + \Delta t B\left[u^{(m)}\right], \quad m = 0, 1, \ldots \tag{III.1}$$

For a fixed *m*, we solve Eq. (III.1) using a finite-difference Fourier spectral method. To do so, we discretize spatially both sides of Eq. (III.1), and then use the discrete Fourier transform to obtain the corresponding system of linear equation in the Fourier space. This is a diagonal system so that it can be solved directly. Finally, we transform back to the real space to obtain the numerical solution to (III.1).

We choose our constant mobility $M(\varepsilon) = 1/\varepsilon$. To stabilize our numerical computations, we vary the two penalty parameters $M_A(\varepsilon)$ and $M_V(\varepsilon)$ in the time iteration (III.1). For instance, we set

$$M_A(\varepsilon, m) = M_V(\varepsilon, m) = 0.1m, \quad \text{(III.2)}$$

and replace $M_A(\varepsilon)$ and $M_V(\varepsilon)$ in (II.7) by $M_A(\varepsilon, m)$ and $M_V(\varepsilon, m)$, respectively. After certain number of steps, say, $m = 1000$, we freeze $M_A(\varepsilon)$ and $M_V(\varepsilon)$ in (III.1).

Algorithm

1. Select a tolerance $\delta > 0$. Select an initial solution $u^{(0)}$ and compute the energy $E_\varepsilon[u^{(0)}]$. Set $m = 0$.

2. Solve Eq. (III.1) for $u^{(m+1)}$ using the Fourier spectral method.

3. Calculate the energy $E_\varepsilon[u^{(m+1)}]$.

4. If $|E_\varepsilon[u^{(m)}] - E_\varepsilon[u^{(m+1)}]| < \delta$ then stop. Otherwise, change *m* to $m + 1$ and go back to Step (2).

IV. COMPUTATIONAL RESULTS

A. Two-Dimensional (2D) Results

We first present our 2D computational results, where the volume and area reduce to the 2D perimeter and area, respectively. We fix the area *V* and select different values of perimeter *A*. For instance, we fix $V = \pi$ and choose *A* to be 2.5*V*, 4*V*, and 5*V*, respectively. For each value *A/V* we run our code. We choose our computational domain to be $\Omega = (-3, 3)^2$ and cover it by a uniform grid of 128×128 grid points. We set $\varepsilon = 0.1$, $\kappa = 1$, $M(\varepsilon) = 0.5$, and $t = 10^{-5}$. The initial phase-field function $u^{(0)} = u^{(0)}(x)$ is taken to represent a circle, ellipse, or "bean".

Figures 1–3 display some of our computational results. In each row of these figures, the first picture is the initial configuration and the last picture is the steady-state solution. The two pictures in between are some intermediate states of *u*. In the red region *u* is 1 and in the blue region *u* is 0. We observe from these computational results a diverse family of minimum-energy configurations which depend on the initial configuration and increase in complexity as the perimeter-to-area ratio increases. In particular, we see clearly from Figures 1 and 2 that the final equilibrium shapes with higher perimeter-to-area ratios have more small pieces that have larger total perimeters.

B. Three-Dimensional (3D) Results

In the 3D computations, we fix the constant area A in the functional E_ε to be 4π, the area of unit sphere, and use the reduced volume $V_{\text{redu}} = V/(4\pi/3)$ as a new parameter, where V the constant volume in the functional E_ε and $4\pi/3$ is the volume of unit ball. We choose the computational domain $\Omega = (-1.5, 1.5)^3$ and cover it by a uniform grid of $128 \times 128 \times 128$ grid points. Our other parameters are $\varepsilon = 0.2$, $\kappa = 1$, $M(\varepsilon) = 0.5$, and $t = 10^{-5}$.

We choose five different types of initial phase-field functions $u^{(0)} = u^{(0)}(x)$. The first four of them are in the form of

$$u^{(0)}(x) = 0.5 + 0.5\tanh\left(\frac{r - \text{dis}(x)}{\varepsilon/3}\right).$$

where the function dis(x) and the parameter r are given by

1. Sphere:

$$\text{dis}(x) = \sqrt{x_1^2 + x_2^2 + x_3^2} \quad \text{and} \quad r = 1,$$

where $x = (x_1, x_2, x_3)$;

2. Prolate:

$$\text{dis}(x) = \sqrt{\left(\frac{x_1}{2}\right)^2 + x_2^2 + x_3^2} \quad \text{and} \quad r = 1;$$

3. Oblate:

$$\text{dis}(x) = \sqrt{x_1^2 + x_2^2 + (2x_3)^2} \quad \text{and} \quad r = 1;$$

4. Parachute:

$$\text{dis}(x) = \sqrt{x_1^2 + x_2^2 + x_3^2} \quad \text{and} \quad r = 1 + \sin\theta,$$

where

$$\theta = \arctan\left(\frac{x_3}{x_1^2 + x_2^2 + 0.01}\right).$$

The last initial phase-field function is chosen to represent a cube:

5. Cube:

$$u^{(0)}(x) = \begin{cases} 1 & \text{if} |x_1| < 1, |x_2| < 1, |x_3| < 1, \\ 0 & \text{otherwise.} \end{cases}$$

We first consider the axisymmetric 3D geometries. In Figure 4, we present the final equilibrium configurations with different reduced volumes and oblate initials. Each row displays a sequence of four snapshots of numerical computations at different times, with the first one being the initial shape and the last one the equilibrium. The small 2D images are cross sections of the corresponding 3D shapes. For the reduced volume $V_{\text{redu}} = 0.667$ (top row), the oblate initial evolves into a discocyte. For $V_{\text{redu}} = 0.5$ (bottom row), the oblate initial shrinks, with the two poles getting closer and then merging, going through a topological change, and finally evolves into a torus.

In Figure 5, we start with a parachute initial. For $V_{\text{redu}} = 0.75$ and 0.60 (top two rows), the equilibriums are parachute shape. Note that a smaller reduced volume corresponds to a smaller open hole at the south pole. Once the reduced volume becomes even smaller (bottom row), the open hole at south pole merges and the equilibrium becomes a concentric sphere.

Figure 6 shows a phase diagram of the axisymmetric 3D equilibriums. There are three curves that correspond to three different initial shapes: prolate, oblate, and parachute. Each curve is the bending energy (defined to be the final minimum energy divided by $8\pi\kappa$) vs. the reduced volume. The 2D cross sections of three representative solutions correspond to the reduced volume $V_{\text{redu}} = 0.8, 0.6, 0.57$, respectively. We observe that, for $V_{\text{redu}} \quad V_{\text{pr}\leftrightarrow\text{ob}} \approx 0.65$, the prolate shape is energetically the most favorable one. For the reduced volume $V_{\text{redu}} \in (V_{\text{ob}\leftrightarrow\text{pa}}, V_{\text{pr}\leftrightarrow\text{ob}}) \approx (0.597, 0.65)$, the oblate shape has the lowest bending energy. If $V_{\text{redu}} \quad V_{\text{ob}\leftrightarrow\text{pa}} \approx 0.597$, the parachute shape is the most stable one. The two critical values of the reduced volume, $V_{\text{ob}\leftrightarrow\text{pa}}$ and $V_{\text{pr}\leftrightarrow\text{ob}}$ agree with the corresponding values reported in [8]. Note that in [8] it is pointed out that, as V_{redu} decreases, the oblate shape finally self-intersects. This will not happen here as our phase-field model can describe the topological changes: the merge of the biconcave region in the center of the oblate and eventually the form of a torus, cf. Figure 4. Similarly, for the parachute branch with V_{redu} decreasing, the two tips in the cross-section view will merge (the open hole at bottom will close), and the parachute shape undergoes a topological change into a concentric sphere, cf. Figure 5.

Note that analytical formulas can be obtained for the sharp-interface limit of some of the phase-field energy minimizers. For instance, if the energy minimizer is a torus, then the distance R from the center of the tube to that of the torus and the radius r of the tube are given by $R = 3/(2\pi V_{\text{redu}})$ and $r = 2V_{\text{redu}}/3$, respectively. respectively. If the energy minimizer is a concentric sphere, we can solve the system of equations $R^2 + r^2 = 1$ and $R^3 - r^3 = V_{\text{redu}}$ to determine the outer and inner radii R and r, respectively.

We now explore more 3D patterns that are the (local) minimizers of our phase-field bending-energy functional with constrained volume and area. In Figure 7, we start from a unit sphere and take five different values of the reduced volume. In each of the five cases, the sphere evolves into a small ball with six handles which become thinner and longer as the reduced volume decreases. In Figure 8, we start from a cubic initial. With three different

values of the reduced volume, we observe even more complicated equilibrium shapes. In Figure 9, the initial shape is an ellipsoid. We observe the topological changes in the relaxation dynamics.

It is clear that the initial shapes determine the final shapes. For instance, final shapes with sphere initials tend to be more rounded or at least more symmetric, cf. Figure 7. Final shapes with ellipsoid initials are more elongated in one direction, same as in the initial ellipsoid, cf. Figure 9. Moreover, we observe that for smaller reduced volumes the final equilibrium surfaces are in general smoother and have larger curvatures. These result from the balance of minimizing the bending energy and satisfying the surface-area and volume constraints. Breaking into more components of surface increases the surface area while keeping the same volume, and also smoothens the surface, reducing the bending energy.

Figure 10 shows the dependence of the final equilibrium bending energy and the corresponding equilibrium shape on the reduced volume.

Finally, in Figures 11 and 12, we display drawings that resemble our computational results to show how the surface is evolved during the relaxation. Figure 11 shows a sequence of cross sections of 6 three-dimensional configurations during the time evolution of relaxation dynamics starting with a sphere. Figure 12 shows a sequence of 6 configurations during the time evolution of relaxation dynamics starting with an ellipsoid. For a high reduced volume, the phase field usually stops evolving at phase 2 or 3. For a low reduced volume, the phase field progresses to phase 5 or 6. Again, with the same volume, equilibrium shapes with lower reduced volumes often have more branches to create larger surface areas. It is interesting to see from Figure 11 that an initial sphere evolves finally to a sphere inside a concentric shell. All of these configurations are spherically symmetric. But many of the intermediate configurations are not spherically symmetric. The existence of such particular intermediate states may depend on the choice of numerical parameter ε that characterizes the width of diffuse surface and the dynamic parameters of penalty $M_A(\varepsilon, m)$ and $M_V(\varepsilon, m)$.

V. CONCLUSIONS

We have constructed a phase-field bending-energy functional with penalty terms enforcing the constraint of surface area and volume. We have also designed and implemented a semi-implicit, finite-difference, Fourier spectral method to solve numerically the gradient flow, minimizing the phase-field functional. The use of penalty terms with dynamic parameters of penalty makes the computation more stable. Our extensive numerical results reveal a wide range of different energy-minimizing configurations. Comparison with existing results indicates that our models and methods are accurate and reliable.

In general, initial shapes determine the final, locally energy-minimizing shapes. With a smaller reduced volume, the final surface breaks up into several components to increase the surface area while keeping the volume fixed. For a larger reduced volume, the final surface often has one component (no break up) but can have large curvatures. Break up and smoothness result from the competition between the minimization of bending energy and the surface-area and volume constraints. High-energy configurations often correspond to

medium values of reduced volume, since for such values no break up is needed to satisfy the constraints but more complicated topologies appear.

We remark that the spontaneous curvature, an important quantity in membrane modeling, can be included approximately in our model and numerical implementation. For instance, we can replace the bending energy term, the κ-term, in (II.1) by [36]

$$E_\varepsilon(u) = \int_\Omega \frac{\kappa}{2\varepsilon} \left[-\varepsilon \Delta u + \frac{1}{\varepsilon} W'(u) - \varepsilon H_0 |\nabla u| \right]^2 \mathrm{d}x,$$

where H_0 is a constant representing the spontaneous curvature, and study the resulting functional E_ε. Note that $\varepsilon |\nabla u|^2 \approx W(u)/\varepsilon$ for small $\varepsilon > 0$. This implies that the terms inside the pair of brackets are approximations to $-\varepsilon \Delta u + W'(u)/\varepsilon - H_0 \sqrt{W(u)}$. The integral of the square of this sum, with an effective parameter H_0, is exactly the bending energy with the spontaneous curvature, proposed as in Eq. (2.1) in [36]. Figure 13 shows our phase-field computational results that include the parameter of spontaneous curvature H_0.

We point out that our phase-field relaxation is a method of steepest descent. Like any such a method, it can only capture locally energy-minimizing states for which suitable initial states are known. Consequently, many local minimizers may not be discovered as the energy landscape can be very complicated. In fact, for a given reduced volume, we have seen from our computations that there are often many different local minimizers of the bending energy functional. Moreover, a method of steepest descent does not in general describe the real dynamics. Therefore, it is often unable to sample all the states to provide the "ensemble average" such as the statistically weighted energy value.

Nevertheless, what we have presented is a first step toward understanding a complicated system. In addition to exploring different surface patterns as it is done in this work, we can apply our relatively simple and reliable computational model and method to study other problems, such as the stability of vesicles [37, 38]. In order for our phase-field approach to be able to treat more realistic systems, however, we have to develop new method to describe the surface fluctuations [39]. These are among the directions we plan to pursue.

Acknowledgments

References

1. Canham PB. J Theor Biol. 1970; 26:61. [PubMed: 5411112]
2. Evans EA. Biophys J. 1974; 14:923. [PubMed: 4429770]
3. Deuling HJ, Helfrich W. J Phys (Paris). 1976; 37:1335.
4. Deuling HJ, Helfrich W. Biophys J. 1976; 16:861. [PubMed: 938726]
5. Evans EA. Biophys J. 1983; 43:27. [PubMed: 6882860]

6. Seifert U. Adv Phys. 1997; 46:13.

7. Helfrich W. Z Naturforsch C. 1973; 28:693. [PubMed: 4273690]

8. Seifert U, Berndl K, Lipowsky R. Phys Rev A. 1991; 44:1182. [PubMed: 9906067]

9. Jülicher F, Seifert U, Lipowsky R. Phys Rev Lett. 1993; 71:452. [PubMed: 10055274]

10. Willmore, T. Riemannian Geometry. Claredon Press; 1993.

11. Gilmer GH, Gilmore W, Huang J, Webb WW. Phys Rev Lett. 1965; 14:491.

12. Collins JB, Levine H. Phys Rev B. 1985; 31:6119.

13. Langer, JS. Directions in Condensed Matter Physics. Grinstein, G.; Mazenko, G., editors. World Scientic; 1986.

14. Gránásy L. J Phys Chem. 1995; 100:10768.

15. Anderson DM, McFadden GB, Wheeler AA. Ann Rev Fluid Mech. 1998; 30:139.

16. Karma A, Kessler D, Levine H. Phys Rev Lett. 2001; 87:045501. [PubMed: 11461627]

17. Boettinger WJ, Warren JA, Beckermann C, Karma A. Annu Rev Materials Res. 2002; 32:163.

18. Chen LQ. Annu Rev Materials Res. 2002; 32:113.

19. Emmerich, H. The Diffuse Interface Approach in Materials Science: Thermodynamic Concepts and Applications of Phase-Field Models. Springer; 2003.

20. Du Q, Liu C, Wang X. J Comput Phys. 2004; 198:450.

21. Biben T, Kassner K, Misbah C. Phys Rev E. 2005; 72:041921.

22. Du Q, Liu C, Wang X. J Comput Phys. 2006; 212:757.

23. Jamet D, Misbah C. Phys Rev E. 2007; 76:051907.

24. Shao D, Rappel WJ, Levine H. Phys Rev Lett. 2010; 105:108104. [PubMed: 20867552]

25. Shao D, Levine H, Rappel WJ. Proc Natl Acad Sci. 2012; 109:6851. [PubMed: 22493219]

26. Camley BA, Zhao Y, Li B, Levine H, Rappel WJ. Phys Rev Lett. 2013; 111:158102. [PubMed: 24160631]

27. Zhao Y, Kwan YY, Che J, Li B, McCammon JA. J Chem Phys. 2013; 139:024111. [PubMed: 23862933]

28. Du Q, Liu C, Ryham R, Wang X. Nonlinearity. 2005; 18:1249.

29. Röger M, Schätzle R. Math Z. 2006; 254:675.

30. Wang, X. PhD thesis. Penn State University; 2005.

31. Campeloa F, Hernández-Machado A. Euro Phys J E. 2006; 20:37.

32. Du Q, Liu C, Wang X. J Comput Phys. 2004; 198:450.

33. Modica L. Archive for Rational Mechanics and Analysis. 1987; 98:123.

34. Sternberg P. Arch Rational Mech Anal. 1988; 101:209.

35. Li B, Zhao Y. SIAM J Applied Math. 2013; 73:1. [PubMed: 24058213]

36. Du Q, Liu C, Ryham R, Wang X. Commun Pure Appl Anal. 2005; 4:537.

37. Jülicher F, Lipowsky R. Phys Rev Lett. 1993; 70:2964. [PubMed: 10053698]

38. Seifert U. Phys Rev A. 1991; 43:6803. [PubMed: 9905030]

39. Karma A, Rappel WJ. Phys Rev E. 1999; 60:3614.
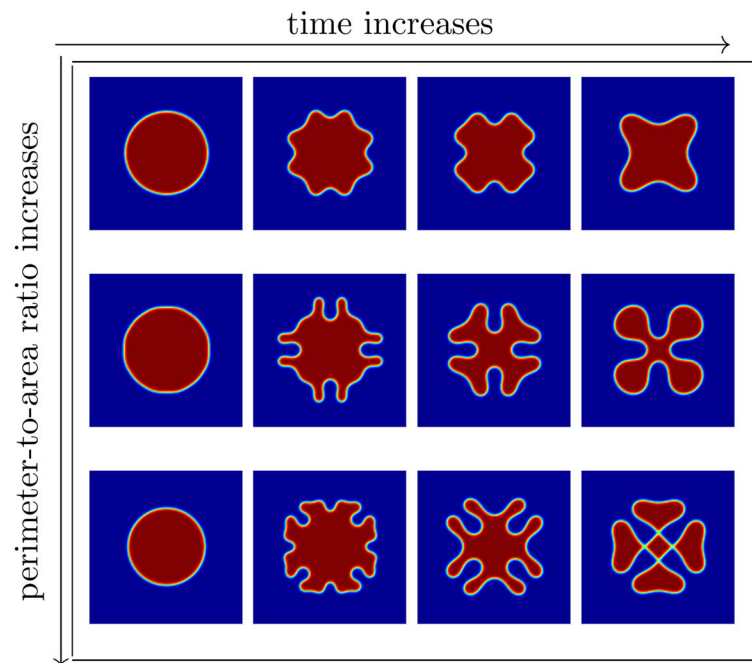
FIG. 1.
(Color online) Configurations started with a circle. Each row displays a sequence of 4 snapshots of numerical computations at different times, with the first being a circle (initial shape) and the last the steady-state configuration. The perimeter-to-area ratios are 2.5, 4, and 5, respectively, from top to bottom.
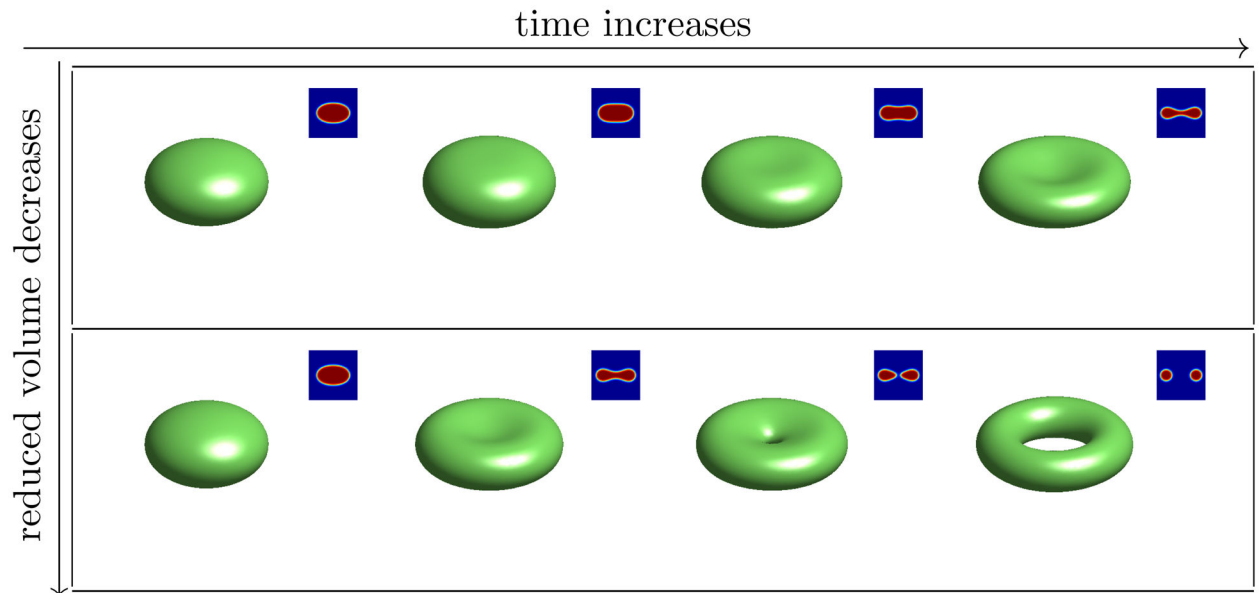
time increases
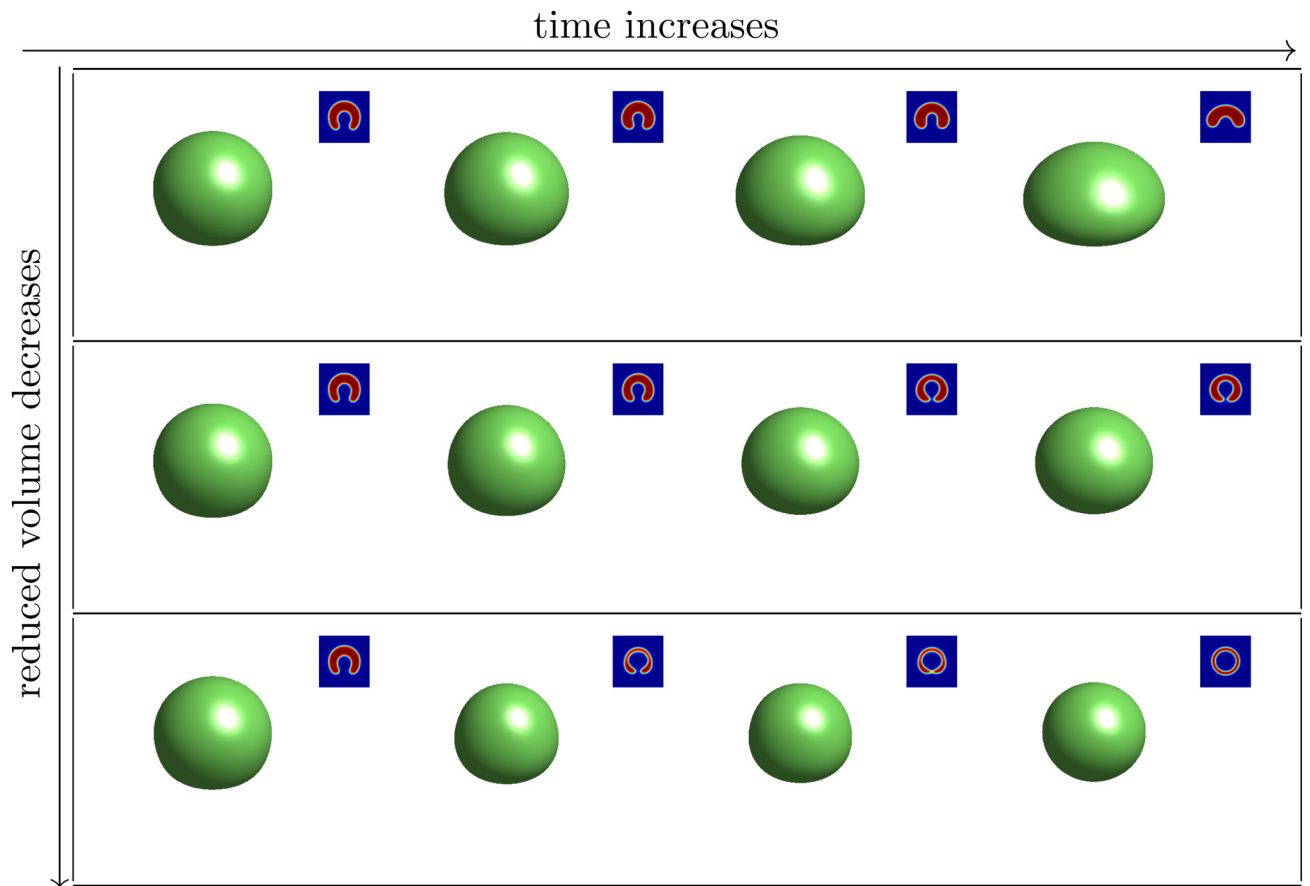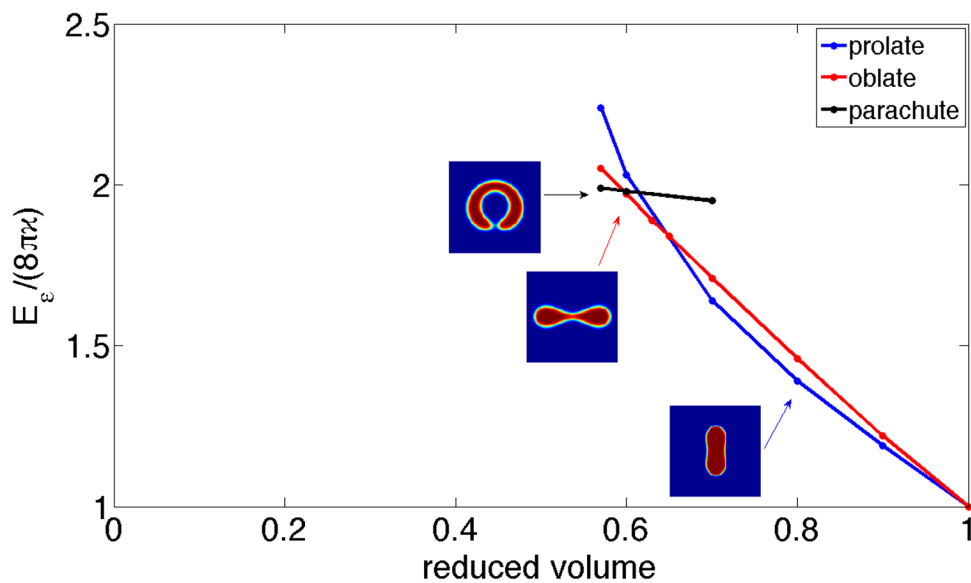
perimeter-to-area ratio increases
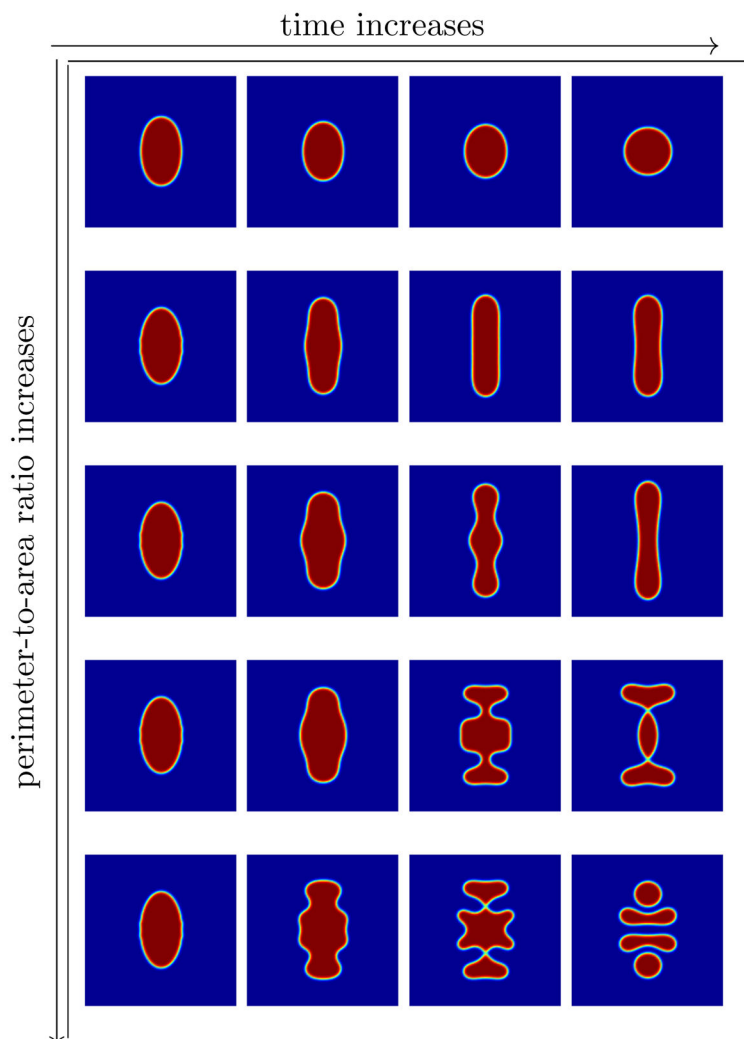
FIG. 2.
(Color online) Configurations started with an ellipse. Each row displays a sequence of 4 snapshots of numerical computations at different times, with the first being an ellipse (initial shape) and the last the steady-state configuration. The perimeter-to-area ratios are 2, 3.5, 4, 5.5, and 6.5, respectively, from top to bottom.
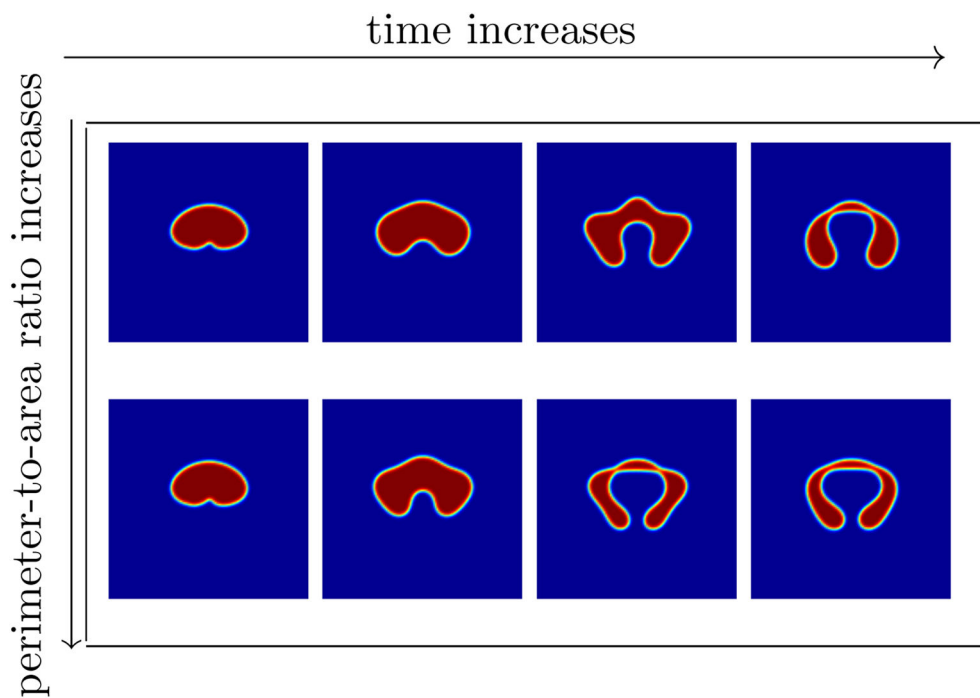
FIG. 3.
(Color online) Configurations started with a "bean". Each row displays a sequence of 4 snapshots of numerical computations at different times, with the first being a "bean" (initial shape) and the last the steady-state configuration. The perimeter-to-area ratios are 7 (top row) and 8 (bottom row), respectively.

FIG. 4.

(Color online) Configurations with different reduced volumes and oblate initials. Each row displays a sequence of four snapshots of numerical computations at different times, with the first being the initial shape and the last the steady-state configuration. Small 2D images are cross sections of the corresponding 3D shapes. The reduced volumes are 0.667 (top) and 0.500 (bottom).

FIG. 5.
(Color online) Configurations with different reduced volumes, started with a parachute. Each row displays a sequence of four snapshots of numerical computations at different times, with the first being the initial shape and the last the steady-state configuration. The reduced volumes are 0.75, 0.60, and 0.25, respectively, from top to bottom.

FIG. 6.
(Color online) The bending energy v.s. reduced volume V_{redu}. The three branches of prolate, oblate, and parachute shapes are displayed. The two critical values of reduced volume from prolate to oblate and from oblate to parachute are $V_{\mathrm{pr}\leftrightarrow\mathrm{ob}} \approx 0.65$ and $V_{\mathrm{ob}\leftrightarrow\mathrm{pa}} \approx 0.597$, respectively. These results agree well with those obtained using the sharp-interface model [8].
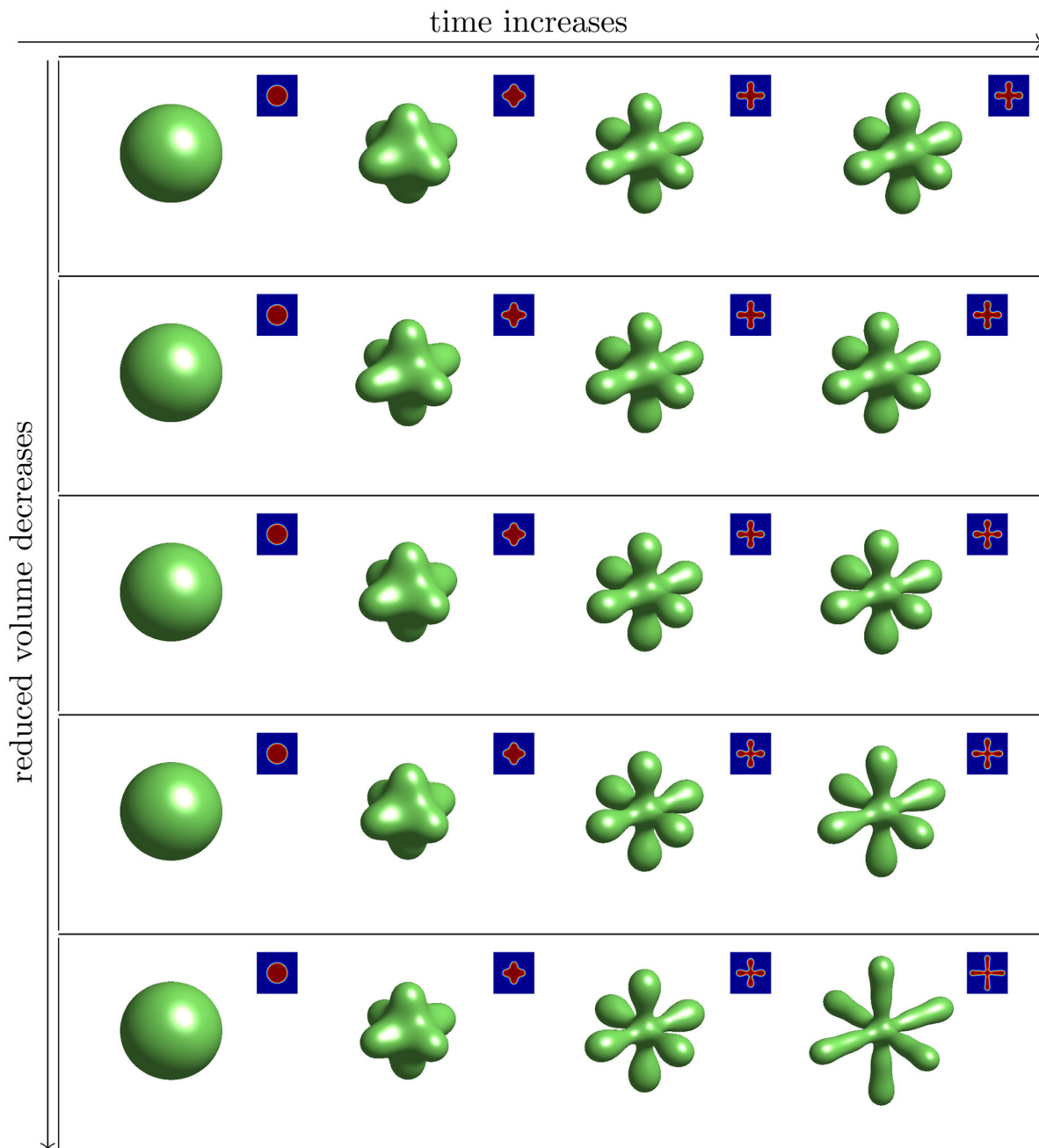
FIG. 7.
(Color online) Configurations with different reduced volumes, all started with a unit sphere. Each row displays a sequence of four snapshots of numerical computations at different times, with the first being an initial unit sphere and the last the steady-state configuration. The reduced volumes are 0.423, 0.411, 0.333, 0.250, and 0.167, respectively, from top to bottom.
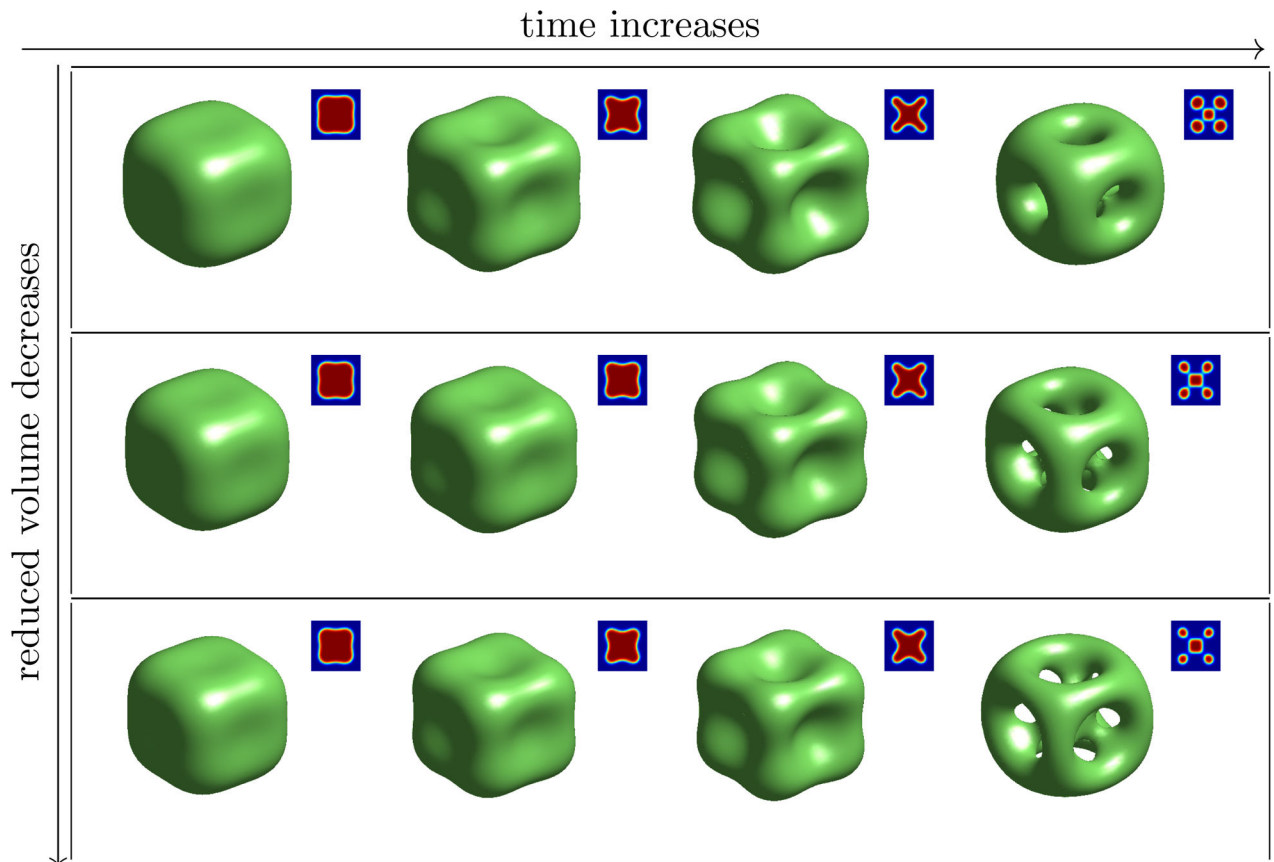
FIG. 8.

(Color online) Configurations with different reduced volumes, all started with a cube. Each row displays a sequence of four snapshots of numerical computations at different times. The reduced volumes are 0.45, 0.35, and 0.25, respectively, from top to bottom.
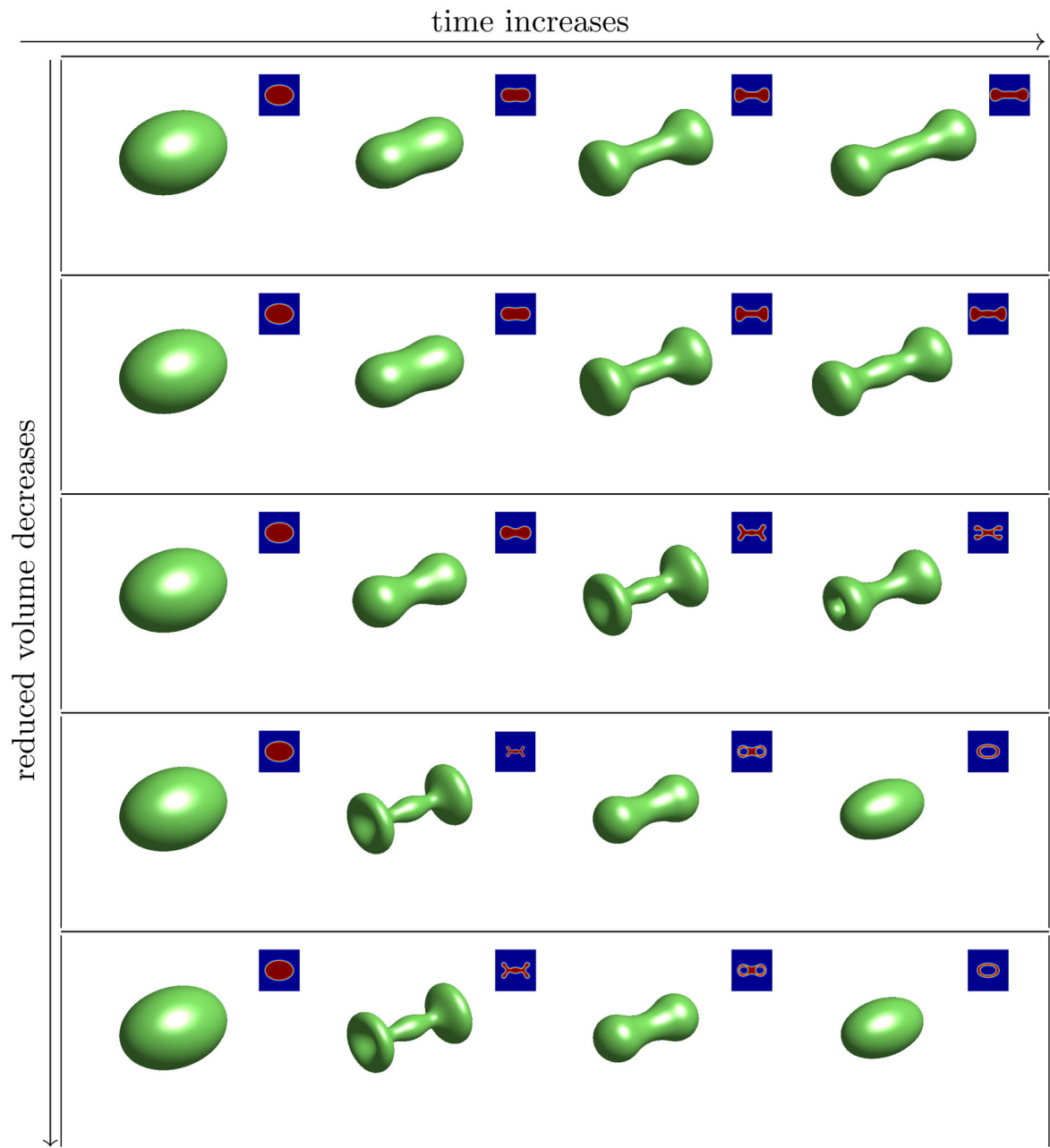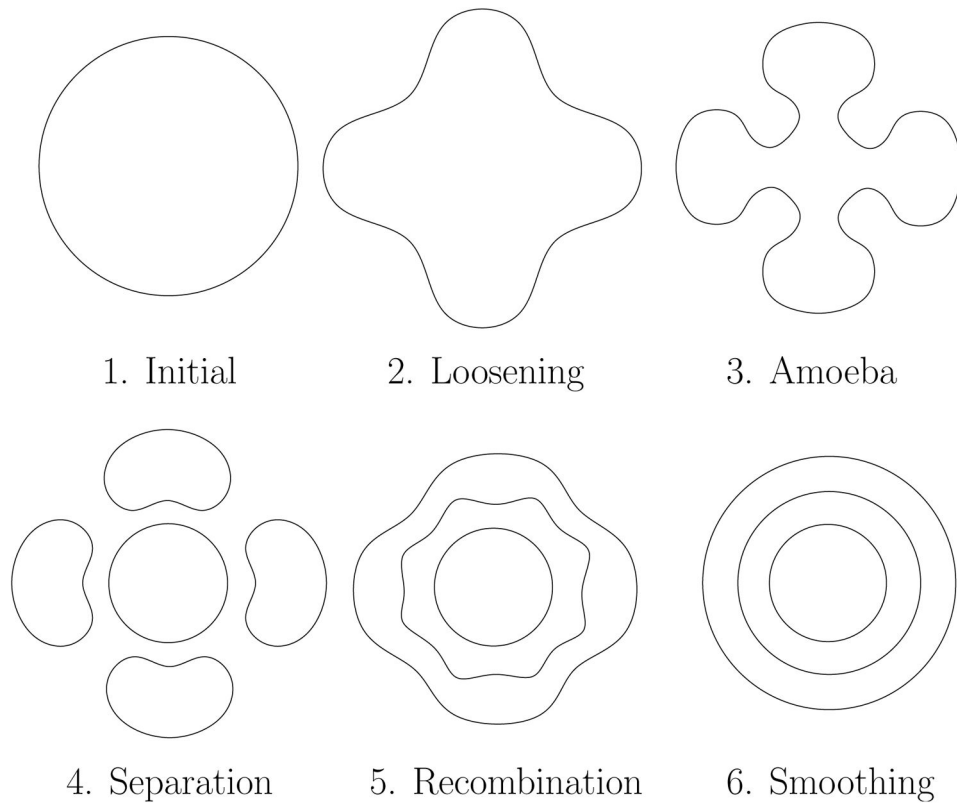
FIG. 9.
(Color online) Configurations with different reduced volumes, all started with an ellipsoid. Each row displays a sequence of four snapshots of numerical computations at different times, with the first being an initial ellipsoid and the last the steady-state configuration. Small 2D images are cross sections of the corresponding 3D shapes. The reduced volumes are 0.600, 0.577, 0.429, 0.333, and 0.328, respectively, from top to bottom.
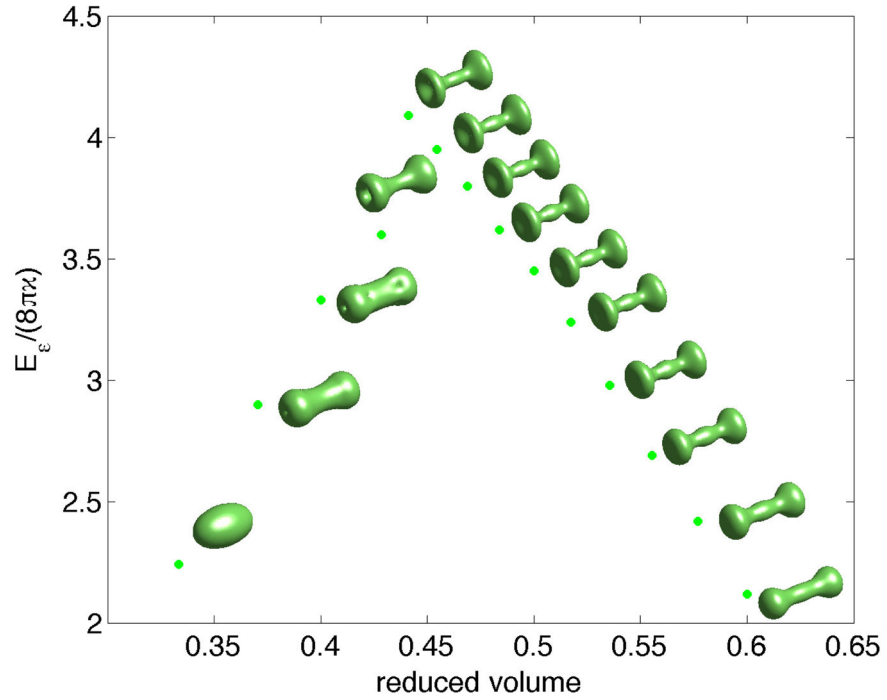
FIG. 10.

(Color online) The dependence of the relaxed (local) minimum energy and the corresponding configurations on the reduced volume. Each initial is an ellipsoid. The reduced volumes of the representative equilibriums are 0.600, 0.577, 0.556, 0.536, 0.517, 0.500, 0.484, 0.469, 0.455, 0.441, 0.429, and 0.333, respectively, from left to right.

FIG. 11.
Cross sections of an evolving surface. Initial profile is a sphere.

1. Loosening

4. Recombination

2. Amoeba

5. Hole Recombination

3. Separation

6. Smoothing
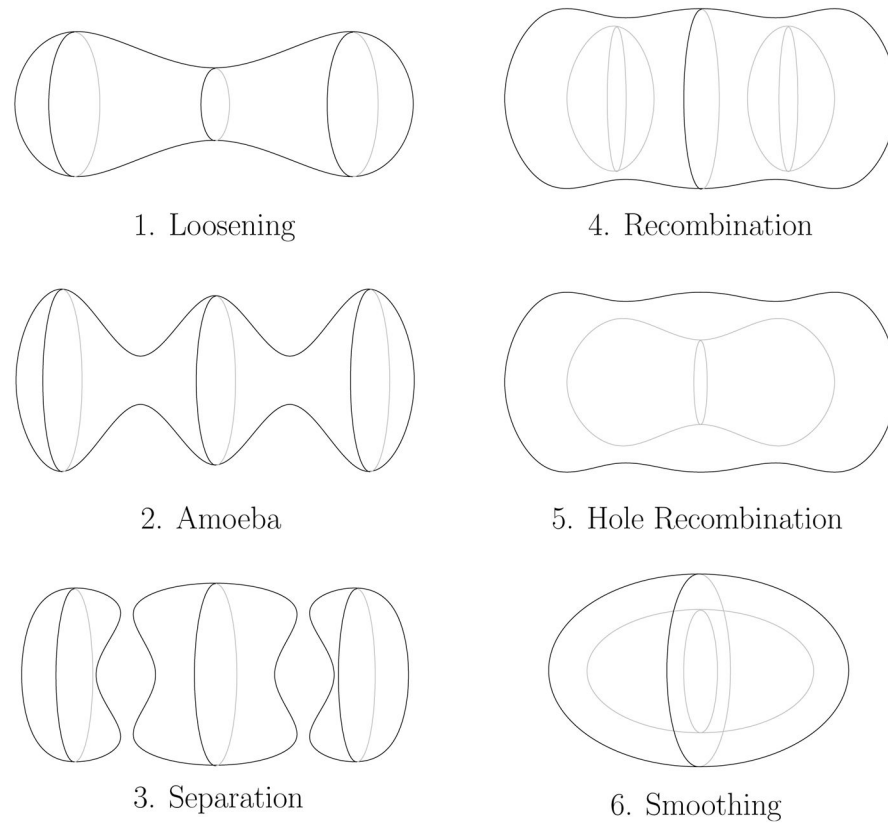
FIG. 12.
Phase-field evolution of a surface. Initial profile is an ellipsoid (not shown here). Grey lines show the boundary of the interior regions and the shape of the back side of the configuration.
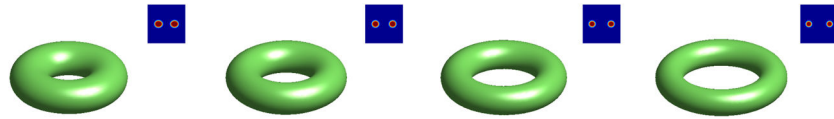
FIG. 13.

(Color online) Equilibrium configurations with different spontaneous curvature $H_0 = 2, 4, 6$, and 8, respectively, from left to right. The reduced volume is fixed to be 0.6.